Onset of inverse magnetic energy transfer in collisionless turbulent plasmas

Z. H. Zhao,[1] Y. Xie,[1] Z. Lei,[1] J. L. Jiao,[1] W. M. Zhou,[2] C. T. Zhou,[3] S. P. Zhu,[4] X. T. He,[1,4] and B. Qiao[1,*]

[1]*Center for Applied Physics and Technology, HEDPS, and SKLNPT, School of Physics, Peking University, Beijing 100871, China*

[2]*Science and Technology on Plasma Physics Laboratory, Research Center of Laser Fusion, China Academy of Engineering Physics, Mianyang 621900, China*

[3]*Center for Advanced Material Diagnostic Technology, Shenzhen Technology University, Shenzhen 518118, China*

[4]*Institute of Applied Physics and Computational Mathematics, Beijing 100094, China*

(Received 11 March 2021; accepted 28 July 2021; published 9 August 2021)

Inverse magnetic energy transfer from small to large scales is a key physical process for the origin of large-scale strong magnetic fields in the universe. However, so far, from the magnetohydrodynamic perspective, the onset of inverse transfer is still not fully understood, especially the underlying dynamics. Here, we use both two-dimensional and three-dimensional particle-in-cell simulations to show the self-consistent dynamics of inverse transfer in collisionless decaying turbulent plasmas. Using the space filtering technique in theory and numerical analyses, we identify magnetic reconnection as the onset and fundamental drive for inverse transfer, where, specifically, the subscale electromotive force driven by magnetic reconnection do work on the large-scale magnetic field, resulting in energy transfer from small to large scales. The mechanism is also verified by the strong correlations in locations and characteristic scales between inverse transfer and magnetic reconnection.

DOI: 10.1103/PhysRevE.104.025204

I. INTRODUCTION

One of the most puzzling problems in the universe is the origin of large-scale strong magnetic fields that exist widely in planets, stars and galaxies [1]. These magnetic fields are of great significance on many astrophysical events [2] such as accretion, star formation, and cosmic rays. In principle, two main processes play key roles in formation of such fields: inverse cascade [3] of magnetic energy from small (seeded kinetic) to large magnetohydrodynamic (MHD) scales that increases the spatial scale of the magnetic field and afterwards the dynamo generally in MHD scale [4–6] that amplifies the field intensity. In addition, the kinetic instabilities may also contribute to amplification of magnetic fields if the pressure anisotropy is excited [7,8].

A large number of investigations [9–11] on inverse cascade have been carried out from the MHD perspective. Three-dimensional MHD simulations show that [12,13] inverse transfer always exists in helical turbulences, where the magnetic helicity keeps conserved [14–16]. For nonhelical turbulences, inverse transfer was not expected to occur in early studies, however, recent high-resolution simulations have also seen it happens in either nonrelativistic [17] or relativistic [18] regimes. This contradiction clearly implies that magnetic helicity is not the decisive condition for onset of inverse transfer. The fundamental drive and essential mechanism of inverse magnetic energy transfer is still not fully understood yet, so far.

However, in astrophysics most seed magnetic fields are generated at small kinetic scale in collisionless or weakly collisional regimes, such as those generated by Biermann battery [19] and Weibel instabilities [20]. Inverse transfer should enable the kinetic-scale seed fields to develop spatial coherent structures on larger and larger scales till into MHD scenario, which are further amplified by turbulent dynamo. Therefore, to give a self-consistent description of the onset and dynamics of inverse transfer requires a kinetic simulation [21–23] that does not depend on a specific closure condition required for MHD.

In this paper, we present two-dimensional (2D) and three-dimensional (3D) kinetic particle-in-cell (PIC) simulations for a collisionless decaying turbulent plasma with random seed magnetic fields and/or flux tubes, where the self-consistent dynamics of inverse magnetic energy transfer is shown. By using the space filtering technique [24] in both theoretical derivations and numerical analyses, we identify magnetic reconnection [25–28] as the fundamental drive for inverse transfer. More essentially, we demonstrate that the subscale convective and Hall electromotive force driven by reconnection do work on large-scale magnetic fields, resulting in energy transfer from small to large scales. We also find that both the locations and the characteristic scales of inverse transfer have strong correlations with those of magnetic reconnection, instead of only the spectral similarity [29–32] got in MHD simulations, which further verifies the mechanism.

II. SIMULATION SETUP

The PIC simulations are performed with the code "EPOCH" [33]. The simulation box is composed of 2048^2 cells in 2D and 512^3 cells in 3D, constituting a domain size $(16\pi d_i)^2$ and $(8\pi d_i)^3$, respectively, where d_i is the ion skin depth. The whole simulation box is filled with a Maxwellian distributed plasma with density n_0 and temperature T_0, where 128 (in 2D) and 4 (3D) macroparticles per cell are used.

*bqiao@pku.edu.cn

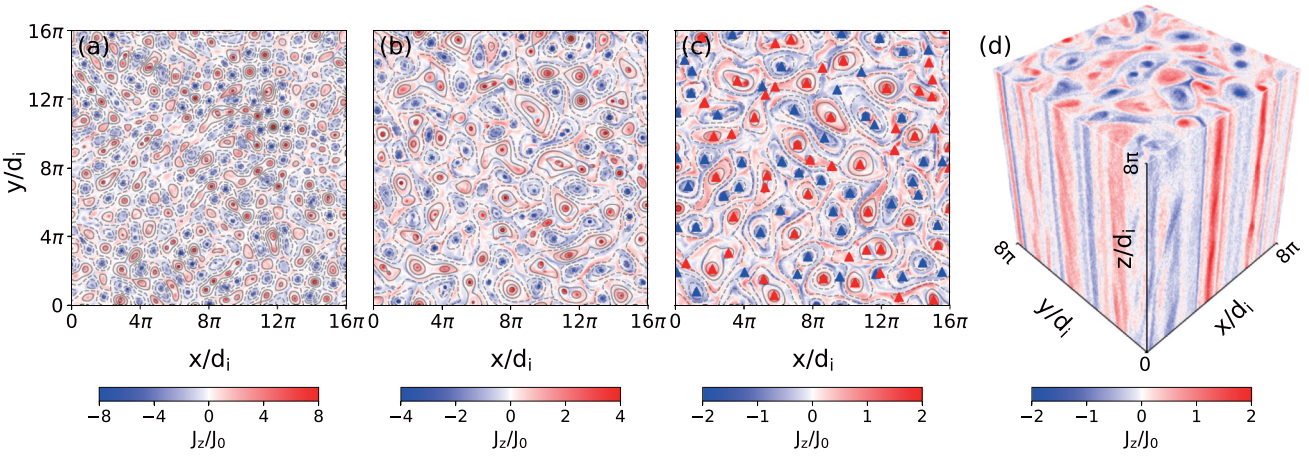

FIG. 1. Distributions of out-of-plane current density J_z (blue-red colors) and magnetic vector potential A_z (contour lines) at times (a) $t = 5$, (b) 15, (c) 40 ω_{ci}^{-1} in 2D, and (d) 20 ω_{ci}^{-1} in 3D simulations of collisionless turbulences with random seed fields. The triangular symbols in panel (c) represent the extreme points (O-points) of A_z with maximum in red and minimum in blue colors.

Due to the limitation of the computational resources, we have also checked the convergence of the simulation by using more particles (8 particles) in the smaller 3D simulation box $[(4\pi d_i)^3]$, where the same main physics are shown. Periodic boundary conditions are taken in all directions. A uniform background magnetic field $\mathbf{B}_z = B_0\hat{z}$ is applied, where B_0 is the normalized strength. The ratio of plasma thermal pressure to magnetic pressure $\beta = n_0T_0/(B_0^2/2\mu_0) = 0.2$ and the Alfvén speed $v_A/c = 0.05$ are chosen. To save computational resources, we choose ion to electron mass ratio $m_i/m_e = 25$, correspondingly, the electron gyration radius becomes $r_{ce}/d_i = 0.09$ and the ratio of plasma frequency to gyration frequency $\omega_{pe}/\omega_{ce} = 4$.

The common method for random seed magnetic field setup in turbulence simulations [34,35] is used, where multiple kinetic-scale magnetic islands are distributed as $\delta B_x = \sum_{m,n} b_{mn} n \sin(k_m x + \psi_{mn})\cos(k_n y + \phi_{mn})$ and $\delta B_y = \sum_{m,n} -b_{mn} m \cos(k_m x + \psi_{mn})\sin(k_n y + \phi_{mn})$. The subindex $m, n \in [l_{\min}, l_{\max}]$ are Fourier mode numbers along x and y directions, and the wave numbers are $k_m = 2\pi m/L$ and $k_n = 2\pi n/L$, where L is the size of simulation box. ψ_{mn} and ϕ_{mn} are random phases. The coefficient $b_{mn} = 2B_0/[(m^2 + n^2)(l_{\max}^2 - l_{\min}^2)]^{1/2}$ is set to satisfy $\langle \delta B_x^2 + \delta B_y^2 \rangle \approx B_0^2$, where $\langle \cdots \rangle$ represents the spatial average operator. In 2D simulations, $l_{\min} = 8$ and $l_{\max} = 16$ are chosen so that the simulated turbulent system initially contains hundreds to thousands of magnetic islands. In 3D simulations, the random field is setting as a straightforward extension of 2D in the z direction to form the flux tubes, which can be used to mimic the elongated current filaments induced by the Weibel-type instabilities occurring widely in the astrophysical counter-streams. Here $l_{\min} = 4$ and $l_{\max} = 8$ are taken. Hereafter, the normalizations with space to d_i, time to ω_{ci}^{-1}, magnetic field to B_0, electric field $E_0 = v_A B_0$, current density $J_0 = en_0 v_A$, energy transfer and dissipation rate to $P_0 = J_0 E_0$ are used for all physical quantities.

III. SIMULATION RESULTS

First, let us show the overall picture of inverse transfer occurring in simulations. Figure 1 plots distributions of out-of-plane current density J_z (blue-red colors) and magnetic vector potential A_z (contour lines) at different times. We see that due to conservation of $|A_z|^2$, the plasma spontaneously evolves to form an ocean of small-scale magnetic islands from initial random seeds, where J_z and A_z are self-organized [Fig. 1(a)]. Afterwards, some neighboring magnetic islands gradually merge together, resulting in enlargement of their scales and decrease of their numbers, see Fig. 1(b) [where the number of magnetic islands is reduced to 1/2 of that in Fig. 1(a)] and Fig. 1(c) (reduced to 1/4). The number and positions of islands are calculated by counting the extreme points of A_z [36], illustrated by the triangular symbols in Fig. 1(c). Further, we see the current densities decrease from Fig. 1(a) to Fig. 1(c) because the turbulence has no external drive. The 3D simulation results in Fig. 1(d) show overall similar picture of inverse transfer. We also see that, in addition to merging, the flux tubes suffer from current-driven kink-mode instabilities in the elongated direction, which enhances interactions between plasmas and magnetic fields.

Figure 2(a) shows magnetic field energy spectra $\mathcal{E}_B(k) = |B(k)|^2$ at various times in 2D simulation, where k is the wave number. We see that the peak wave number k_{peak} [where $\mathcal{E}_B(k)$ has the maximum value] decreases with time, i.e., Bose-Einstein condensation [37–39] in low-k modes. This means the magnetic field energy moves gradually from small to large scales, i.e., inverse magnetic energy transfer. Furthermore, for $k < k_{\text{peak}}$ in the subinertial range, we see that the growth of field energy slows down with time, indicating that inverse transfer efficiency drops with time in such decaying turbulence, and the spectra eventually evolves to have a fitting $k^{3.8}$, which is close to the k^4 Batchelor spectrum, in agreement with the causality requirement $\nabla \cdot B = 0$ [40]. While in the inertial range $k > k_{\text{peak}}$, the spectral converges to $k^{-2.5}$, which is significantly deeper than $k^{-2.0}$ of weak turbulence in MHD [17,18,30], but close to $k^{-8/3}$ obtained in kinetic turbulence simulations [41]. The inset shows that the energy spectra of 2D and 3D are highly similar, except for some minor spectral index differences. Note that the Goldreich-Sridhar spectrum $k^{-5/3}$ [42] is expected to appear when $k_{\text{peak}} d_i$ drops below

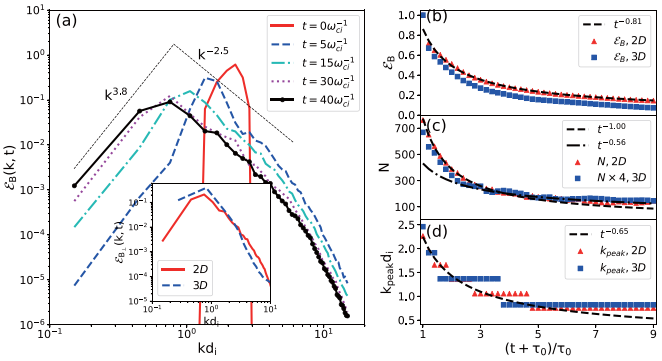

FIG. 2. (a) Magnetic field energy spectra $\mathcal{E}_B(k) = |B(k)|^2$ at various times in 2D simulation, inset shows the comparison of 2D and 3D energy spectra at $t = 40\omega_{ci}^{-1}$; (b) the total field energy $\mathcal{E}_B = \Sigma_k |B_k|^2$ in 2D and 3D; (c) the number of magnetic islands (2D) and flux tubes (3D) N, where the 3D results are multiplied by a factor of 4 because the spatial lengths in the 3D simulation are reduced by 2 times of those in 2D in both x and y direction (the magnetic reconnection and the corresponding inverse cascade occur dominantly in this perpendicular (x, y) plane); (d) the peak wave number $k_{\rm peak}$ evolving with time $(t + \tau_0)/\tau_0$ in 2D and 3D, where $\tau_0 = 5\omega_{ci}^{-1}$.

0.1, indicating that our simulation has not yet entered into the completely MHD-scale turbulent state.

Figures 2(b)–2(d) show, respectively, the total magnetic field energy $\mathcal{E}_B = \Sigma_k |B_k|^2$, the number of magnetic islands (2D) and flux tubes (3D) N, and $k_{\rm peak}$ evolving with time $(t + \tau_0)/\tau_0$ in both 2D and 3D, where τ_0 refers to the time interval for N drops by half of that at initial time. From Figs. 1(a)–1(c), we obtain averagely $\tau_0 \approx 5\omega_{ci}^{-1}$, which corresponds to a reconnection rate $\beta_{\rm rec,0} = R_0/v_A\tau_0 \approx 0.14$ (R_0 is the average initial island radius), close to the typical value 0.1 of collisionless reconnections [43,44]. We see that the self-similarity of inverse transfer also keeps in collisionless turbulent plasmas, where all three physical quantities show a power-law decay whether in 2D or 3D, although their power-law indexes are slightly deviated from those in MHD [30]. This is because that the self-organization process of magnetic reconnection has nothing to do with the specific dissipation mechanisms, regardless of whether in collisional MHD or collisionless kinetic regimes.

Next, we analyze the simulation results in more details to give the fundamental drive and essential mechanism of inverse transfer. We employ the space-filter approach [45–49] with the low-pass filtered field as $\widetilde{\mathbf{U}}(\mathbf{x}, t) \equiv \int d\mathbf{r} \mathbf{G}_l(\mathbf{x} - \mathbf{r})\mathbf{U}(\mathbf{r}, t)$, where $\mathbf{U}(\mathbf{x}, t)$ is any scalor or vector field, $\mathbf{G}_l$ is the filter (convolution kernel), so that $\widetilde{\mathbf{U}}$ only contains information at scale length $> l$. The normalized boxcar window filter [46] is used, and other filter functions (e.g., Gaussian kernel) give similar results. For mass dependence, the mass-weighted-filter (Favre filter [50]) is taken as $\widehat{\mathbf{\Phi}} \equiv n\widetilde{\mathbf{\Phi}}/\widetilde{n}$ with n number density. In 3D simulations, the isotropic filtering kernel with the same scale length l is used here for all three dimensions. We have checked the results with the anisotropic kernel function with $l_\perp$ and $l_\parallel$, which show that in the highly anisotropic flux-tubes, the filtering is insensitive to $l_\parallel$ in the elongated direction and resultantly an isotropic kernel $l_\parallel = l_\perp$ is sufficient to show the main physics of inverse cascades here. From the combination of Faraday's, Ampere's, and Ohm's laws, we obtain that the evolution of the filtered electromagnetic field energy at scale length $> l$ obeys [47,48]

$$\frac{\partial}{\partial t}\left(\frac{1}{2}\frac{\widehat{\mathbf{B}}^2}{\mu_0} + \frac{1}{2}\epsilon_0\widehat{\mathbf{E}}^2\right) + \nabla\cdot\left(\frac{1}{\mu_0}\widehat{\mathbf{E}}\times\widehat{\mathbf{B}}\right) = -\widehat{\mathbf{J}}\cdot\widehat{\mathbf{E}}, \tag{1}$$

$$\widehat{\mathbf{E}} = -\left(\widehat{\mathbf{u}}\times\widehat{\mathbf{B}} - \widehat{\mathbf{J}}\times\widehat{\mathbf{B}}/e\widetilde{n}\right) - \left(\mathcal{T}_{\mathbf{u}\times\mathbf{B}} - \mathcal{T}_{\mathbf{J}\times\mathbf{B}}\right) - \left(\frac{m_e}{e}\frac{d\widetilde{\mathbf{u}}_e}{dt} + \frac{1}{e\widetilde{n}}\nabla\cdot\widetilde{\mathbf{P}}\right). \tag{2}$$

Eqs. (1) and (2) together describe the evolution of electromagnetic field energy at scale length $> l$. We see that, in addition to the original counterparts of all physical quantities at the same scale length $> l$, two new subscale terms (scale length $< l$) appear, namely, the subscale convective electromotive force $\mathcal{T}_{\mathbf{u}\times\mathbf{B}} = \widehat{\mathbf{u}\times\mathbf{B}} - \widehat{\mathbf{u}}\times\widehat{\mathbf{B}}$ and the subscale Hall electromotive force $\mathcal{T}_{\mathbf{J}\times\mathbf{B}} = (\widehat{\mathbf{J}\times\mathbf{B}} - \widehat{\mathbf{J}}\times\widehat{\mathbf{B}})/e\widetilde{n}$. Note that if no filter operation is used, i.e., $l = 0$, these two terms disappear.

In nonrelativistic magnetized plasmas, the electric field energy is much smaller than the magnetic field, so we ignore $\epsilon_0\widehat{\mathbf{E}}^2/2$ in Eqs. (1) and (2). Then we see three source or sink terms do work $-\widehat{\mathbf{J}}\cdot\widehat{\mathbf{E}}$ on magnetic fields. The first term $\mathcal{F}_l = (\widehat{\mathbf{u}}\times\widehat{\mathbf{B}})\cdot\widehat{\mathbf{J}}$ represents the energy conversion caused by large-scale field-plasma interactions, leading to magnetic field compression/stretching, which plays a dynamolike role in small scale converting kinetic to magnetic energy and vice versa. The second term $\mathcal{T}_l = \mathcal{T}_{l1} + \mathcal{T}_{l2} = \mathcal{T}_{\mathbf{u}\times\mathbf{B}}\cdot\widehat{\mathbf{J}} - \mathcal{T}_{\mathbf{J}\times\mathbf{B}}\cdot\widehat{\mathbf{J}}$ is the cross-scale energy transfer driven by the subscale electromotive forces, where a positive (negative) value indicates an inverse (direct) energy transfer, resulting in formation of large-scale magnetic fields. Last, $\mathcal{D}_l = \mathcal{D}_{l1} + \mathcal{D}_{l2} = \frac{m_e}{e}\frac{d\widetilde{\mathbf{u}}_e}{dt}\cdot\widehat{\mathbf{J}} + \frac{1}{e\widetilde{n}}\nabla\cdot\widetilde{\mathbf{P}}\cdot\widehat{\mathbf{J}}$ corresponds to the nonideal energy dissipation, where $\mathcal{D}_{l1}$ and $\mathcal{D}_{l2}$ are driven by the electron inertia and stress tensors. If $l = 0$, $\mathcal{T}_{l=0} = 0$, while $\mathcal{D}_{l=0} \approx -\mathcal{D}_e = -\gamma_e[\mathbf{J}\cdot(\mathbf{E} + \mathbf{v}_e\times\mathbf{B}) - \rho_e(\mathbf{v}_e\cdot\mathbf{E})]$, the Lorentz invariant scalar quantity [51] being used for characterization of local energy dissipation of collisionless reconnection [52] at $l < d_i$. In other words, D_l can be regarded as energy dissipation of magnetic reconnection in a large-scale area including both upstream and downstream regions instead of only localized reconnection points.

Figures 3(a)–3(c), respectively, plot distributions over scale lengths l of $\mathcal{F}_l$, $\mathcal{T}_l$, and $\mathcal{D}_l$. Both $\mathcal{F}_l$ and $\mathcal{D}_l$ show mostly negative values, leading to decrease of the field energy with scale length $> l$, however, $\mathcal{T}_l$ show positive values [Fig. 3(b)], resulting in inverse transfer of magnetic energy from subscales ($< l$) to the large scale ($> l$). From the sum of them shown in Fig. 3(d), we see that the magnetic energies in a large scale with $l > 2d_i$ always show positive values and the characteristic scale length where the peak value of $\mathcal{F}_l + \mathcal{T}_l + \mathcal{D}_l$ locates, $l_{\rm peak}$, increases with time [see also Fig. 3(f)], which both indicates that the field energy is transferred from small to large scales, resulting in developing of large-scale coherent field structures. The insets show consistencies of 2D and 3D simulations, where the deeper $\mathcal{F}_l$ in 3D indicates stronger plasma-field interaction, and if dynamo exists, $\mathcal{F}_l$ even provides a positive value. In view of these, we conclude that increase of magnetic energy in large scales is mostly due to cross-scale inverse transfer driven by the subscale elec-

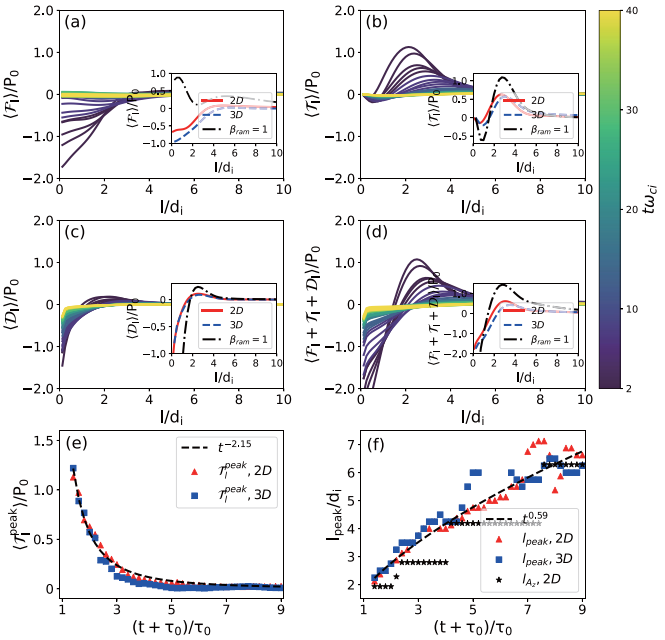

FIG. 3. Distributions over scale lengths l of three source and sink terms in Eqs. (1) and (2) at different times: (a) field-plasma interaction $\mathcal{F}_l$, (b) cross-scale energy transfer $\mathcal{T}_l$, (c) nonideal energy dissipation $\mathcal{D}_l$, and (d) $\mathcal{F}_l + \mathcal{T}_l + \mathcal{D}_l$, where the inset figures show comparisons of 2D and 3D results at $t = 5\omega_{ci}^{-1}$ and all values are multiplied by a factor of 100. (e, f) Time evolutions of the peak $\mathcal{T}_l^{\text{peak}}$ and the corresponding l_{peak} as well as the characteristic scale length l_{A_z} of A_z.

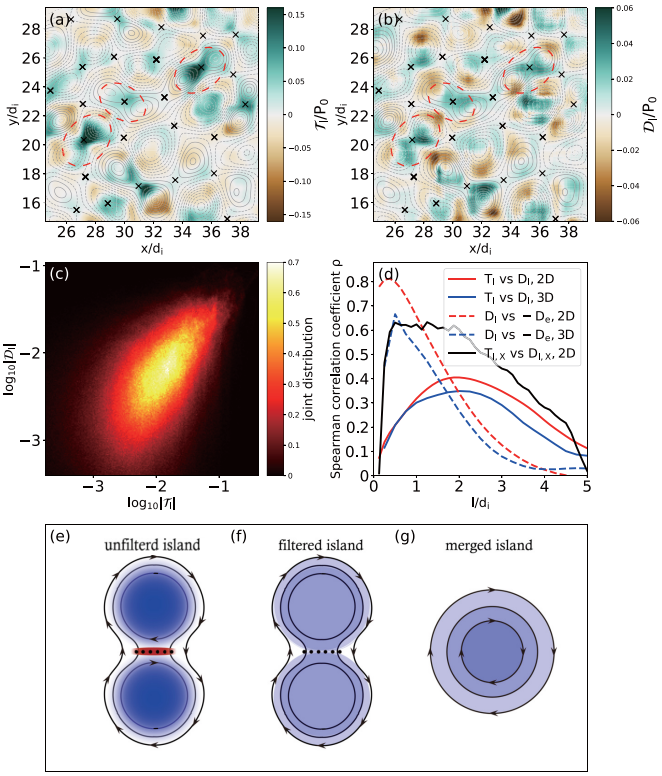

FIG. 4. [(a), (b)] Spatial distributions of $\mathcal{T}_l$ and $\mathcal{D}_l$ in a portion area of the simulation at $t = 5\omega_{ci}^{-1}$, where $l = 2d_i$ is chosen, contour lines show A_z, cross symbols represent the saddle points (X-points) in field topology. (c) Joint distribution of $\log|\mathcal{T}_{l=2d_i}|$ and $\log|\mathcal{D}_{l=2d_i}|$. (d) The Spearmann rank correlation coefficients ρ between $\mathcal{T}_l$ and $\mathcal{D}_l$, $\mathcal{D}_l$ and $-\mathcal{D}_e$, $\mathcal{T}_{l,X}$ and $\mathcal{D}_{l,X}$ at different l. (e–g) Schematic physical picture showing how magnetic reconnection drives inverse transfer from the simple coalescence process of two magnetic islands.

tromotive force $\mathcal{T}_l$. Furthermore, for the decaying turbulence here with no fluid drives $\beta_{\text{ram}} = \frac{1}{2}\rho u_{\text{rms}}^2/(B_0^2/2\mu_0) = 0$, the absolute intensities of all terms decrease with time, and a relatively slow inverse transfer occurs. If adding a fluid drive (such as $\beta_{\text{ram}} = 1$), i.e., initial random velocity field $u_{\text{rms}} \neq 0$, both the magnetic reconnection and inverse cascade rates significantly increase, see insets of Figs. 3(a)–3(d). In the context of magnetic reconnection, the reason is that the fluid drive accelerates the inflow of the magnetic field, thus speeding up the reconnection. To show how the large-scale fluid drive promote the inverse energy transfer and field dynamo processes, a self-consistent combination of both the kinetic PIC simulation and the MHD simulation (and/or a hybrid fluid-PIC simulation) is required, which will be studied in the near future.

Temporal evolutions of the peak intensity $\mathcal{T}_l^{\text{peak}}$ and the corresponding scale length l_{peak} of, respectively, 2D and 3D are shown in Figs. 3(e) and 3(f). $\mathcal{T}_l^{\text{peak}}$ shows a fitting power of $t^{-2.15}$, which is basically consistent with our theory since $\mathcal{T}_{l1} = \mathcal{T}_{\mathbf{u}\times\mathbf{B}}\cdot\widehat{\mathbf{J}} \propto B^3/L \propto t^{-2}$ and $\mathcal{T}_{l2} = -\mathcal{T}_{\mathbf{J}\times\mathbf{B}}\cdot\widehat{\mathbf{J}} \propto B^3/L^2 \propto t^{-2.5}$. More importantly, see Fig. 3(f), l_{peak}, the scale where the large-scale magnetic energy starts to increase, is almost identical to the characteristic scale l_{A_z} of magnetic islands in 2D and flux tubes in 3D (obtained by Fourier transform of A_z) at various times, which both show a fitting of $t^{0.6}$. It is also worth noting that $\mathcal{D}_l$ [Fig. 3(c)] dominates at $l < d_i$, in consistence with our theoretical analysis above for collisionless reconnection. So, all of these indicate a high correlation of inverse transfer with magnetic reconnection.

To further prove that inverse transfer is induced by magnetic reconnection, spatial distributions of $\mathcal{T}_l$ and $\mathcal{D}_l$ at $t = 5\omega_{ci}^{-1}$ are plotted in Figs. 4(a) and 4(b), where $l = 2d_i$ is chosen, identical to the characteristic scale length of magnetic islands. We see a pronounced spatial correlation exists between $\mathcal{T}_l$ and $\mathcal{D}_l$ (see the regions circled in red), and almost all inverse transfers (in green color) occur at the locations exactly around the reconnection points (see contours of A_z and X points marked by the cross symbols). The joint distribution of $\log|\mathcal{T}_l|$ and $\log|\mathcal{D}_l|$ in Fig. 4(c) also confirms such intuitive correlation. For quantitative description of this correlation, we plot the Spearmann rank correlation coefficients ρ between $\mathcal{T}_l$ and $\mathcal{D}_l$ (solid), and $\mathcal{D}_l$ and $-\mathcal{D}_e$ (dashed) varying with l in Fig. 4(d). Obviously, $\mathcal{D}_l$ and $-\mathcal{D}_e$ show a high correlation with $\rho \approx 0.8$ (in 2D) and 0.65 (in 3D) at small scale $l < d_i$, and with the increase of l, ρ drops heavily. Further, $\mathcal{T}_l$ and $\mathcal{D}_l$ show a moderately strong correlation with the peak $\rho \approx 0.4$ (in 2D) and 0.36 (in 3D) at $l \approx 2d_i$, which is approximately equal to the characteristic scale length of magnetic islands, see also Fig. 3(f). Furthermore, there exists an even stronger correlation between $\mathcal{T}_l$ and $\mathcal{D}_l$ at X points with $\rho \approx 0.6$ (solid black line), which is a more pronounced evidence that magnetic reconnection triggers inverse cascade. We have checked

these correlations at other times (such as $t = 15$ and $40\ \omega_{ci}^{-1}$), which show the similar physics.

Last, we take the simple coalescence process of two magnetic islands as example, shown in Figs. 4(e)–4(g), to give a schematic physical picture to understand how magnetic reconnection drives inverse transfer. The two magnetic islands with the same inward current (blue color) are attracted to each other by the $\mathbf{J} \times \mathbf{B}$ force [unfiltered islands, Fig. 4(e)], resulting in formation of a Harris-like current sheet in the outward direction (red color) in the central small scale with $l < d_i$ and eventually occurrence of magnetic reconnection. As a result, an out-of-plane reconnection electric field $\mathbf{E}$ (black dots) is induced, which dissipates the magnetic energy because generally $-\mathbf{J} \cdot \mathbf{E} < 0$. However, if from the large-scale perspective (islands after filtering with $l = 2d_i$ here), see Fig. 4(f), the Harris-like current sheet disappears, and two magnetic islands becomes like one whole peanut-shaped island [18] with the same inward current (blue). As a result, when magnetic reconnection occurs, from the large-scale view we see that the total work $-\widehat{\mathbf{J}} \cdot \widehat{\mathbf{E}} > 0$ [also see Fig. 2(d)], leading to inverse transfer. More exactly, as we analyzed above, the subscale electromotive force induced by reconnection contributes to this cross-scale energy transfer. Correspondingly, the shape of the large magnetic island eventually self-evolves from peanut to commonly circle with the smallest average curvature [Fig. 4(g)]. In other words, from a small-scale view, magnetic reconnection (energy dissipation) occurs, and from a large-scale view, magnetic islands reorganize and expansion (inverse transfer) are observed.

IV. SUMMARY AND DISCUSSION

In summary, we have self-consistently identified that magnetic reconnection is the fundamental drive for inverse magnetic energy transfer in collisionless decaying turbulences. The subscale electromotive force $\mathcal{T}_l$ driven by magnetic reconnection do work on the large-scale magnetic fields, resulting in field energy transfer from small to large scales and consequently appearance of large-scale coherent structures. We also find that both the locations and the characteristic scales of inverse transfer have strong correlations with those of magnetic reconnection, instead of only the spectral similarity [29–32] got in MHD simulations, which further verifies the mechanism.

In a more realistic astrophysical case, the fluid drive from the large-scale environment may significantly accelerate the inverse cascade process shown here, and the dynamo effect becomes dominant as well in the large fluid scale, whose modeling requires a self-consistent combination of both the kinetic PIC and MHD simulations and/or a hybrid fluid-PIC simulation.

ACKNOWLEDGMENTS

This work was supported by Science Challenge Project, No. TZ2018005; National Natural Science Foundation of China, Grants No. 11825502, No. 11921106, and No. 12075014; the Strategic Priority Research Program of Chinese Academy of Sciences Grant No. XDA25050900; the National Key R & D Program of China, Grant No. 2016YFA0401100. B.Q. acknowledges support from National Natural Science Funds for Distinguished Young Scholar, Grant No. 11825502. The simulations wer carried out on the Tianhe-2 supercomputer at the National Supercomputer Center in Guangzhou.

[1] R. M. Kulsrud and E. G. Zweibel, Rep. Prog. Phys. **71**, 046901 (2008).
[2] A. Brandenburg and K. Subramanian, Phys. Rep. **417**, 1 (2005).
[3] D. Ryu, D. R. G. Schleicher, R. A. Treumann, C. G. Tsagas, and L. M. Widrow, Space Sci. Rev. **166**, 1 (2012).
[4] M. Steenbeck, F. Krause, and K.-H. Rädler, Z. Naturforschg. **21**, 369 (1966).
[5] A. Brandenburg, D. Sokoloff, and K. Subramanian, Space Sci. Rev. **169**, 123 (2012).
[6] D. Ryu, H. Kang, J. Cho, and S. Das, Science **320**, 909 (2008).
[7] D. Falceta-Goncalves and G. Kowal, Astrophys. J. **808**, 65 (2015).
[8] D. A. St-Onge and M. W. Kunz, Astrophys. J. Lett. **863**, L25 (2018).
[9] A. Pouquet and G. S. Patterson, J. Fluid Mech. **85**, 305 (1978).
[10] D. Biskamp and U. Bremer, Phys. Rev. Lett. **72**, 3819 (19944).
[11] D. Biskamp and W.-C. Müller, Phys. Rev. Lett. **83**, 2195 (1999).
[12] M. Christensson, M. Hindmarsh, and A. Brandenburg, Phys. Rev. E **64**, 056405 (2001).
[13] A. Brandenburg, Astrophys. J. **550**, 824 (2001).
[14] U. Frisch, A. Pouquet, J. Léorat, and A. Mazure, J. Fluid Mech. **68**, 769 (1975).
[15] D. Fyfe and D. Montgomery, J. Plasma Phys. **16**, 181 (1976).
[16] A. Pouquet, J. Fluid Mech. **88**, 1 (1978).
[17] A. Brandenburg, T. Kahniashvili, and A. G. Tevzadze, Phys. Rev. Lett. **114**, 075001 (2015).
[18] J. Zrake, Astrophys. J. Lett. **794**, L26 (2014).
[19] L. Biermann, Z. Naturforsch., A **5**, 65 (1950).
[20] E. S. Weibel, Phys. Rev. Lett. **2**, 83 (1959).
[21] G. Ganguli, L. Rudakov, W. Scales, J. Wang, and M. Mithaiwala, Phys. Plasmas **17**, 052310 (2010).
[22] O. Chang, S. P. Gary, and J. Wang, Astrophys. J. **800**, 87 (2015).
[23] G. Chatterjee, K. M. Schoeffle, P. K. Singh, A. Adak, A. D. Lad, S. Sengupta, P. Kaw, L. O. Silva, A. Das, and G. R. Kumar, Nat. Commun. **8**, 15970 (2017).
[24] M. Germano, J. Fluid Mech. **238**, 325 (1992).
[25] P. A. Sweet, Nuovo Cimento Suppl. **8**, 188 (1958).
[26] E. N. Parker, Astrophys. J., Suppl. Ser. **8**, 177 (1963).
[27] E. G. Zweibel and M. Yamada, Annu. Rev. Astron. Astrophys. **47**, 291 (2009).
[28] M. Yamada, R. Kulsrud, and H. Ji, Rev. Mod. Phys. **82**, 603 (2010).
[29] P. Olesen, Phys. Lett. B **398**, 321 (1997).

[30] M. Zhou, P. Bhat, N. F. Loureiro, and D. A. Uzdensky, Phys. Rev. Research **1**, 012004(R) (2019).
[31] M. Zhou, N. F. Loureiro, and D. A. Uzdensky, J. Plasma Phys. **86**, 535860401 (2020).
[32] P. Bhat, M. Zhou, and N. F. Loureiro, Mon. Not. R. Astron. Soc. **501**, 3074 (2020).
[33] T. D. Arber, Plasma Phys. Controlled Fusion **57**, 113001 (2015).
[34] C. Dong, L. Wang, Y. M. Huang, L. Comisso, and A. Bhattacharjee, Phys. Rev. Lett. **121**, 165101 (2018).
[35] L. Comisso and L. Sironi, Phys. Rev. Lett. **121**, 255101 (2018).
[36] S. Servidio, W. H. Matthaeus, M. A. Shay, P. A. Cassak, and P. Dmitruk, Phys. Rev. Lett. **102**, 115003 (2009).
[37] L. M. Smith and V. Yakhot, J. Fluid Mech. **274**, 115 (1994).
[38] J. Paret and P. Tabeling, Phys. Rev. Lett. **79**, 4162 (1997).
[39] A. O. Korotkevich, Phys. Rev. Lett. **101**, 074504 (2008).
[40] R. Durrer and C. Caprini, J. Cosmol. Astropart. Phys. **2003**, 010 (2003).
[41] Y. Yang, M. Wan, W. H. Matthaeus, L. Sorriso-Valvo, T. N. Parashar, Q. Lu, Y. Shi, and S. Chen, Mon. Not. R. Astron. Soc. **482**, 4933 (2019).
[42] P. Goldreich and S. Sridhar, Astrophys. J. **438**, 763 (1995).
[43] Y.-H. Liu, M. Hesse, F. Guo, W. Daughton, H. Li, P. A. Cassak, and M. A. Shay, Phys. Rev. Lett. **118**, 085101 (2017).
[44] P. A. Cassak, Y.-H. Liu, and M. A. Shay, J. Plasma Phys. **83**, 715830501 (2017).
[45] S. Chen, R. E. Ecke, G. L. Eyink, M. Rivera, M. Wan, and Z. Xiao, Phys. Rev. Lett. **96**, 084502 (2006).
[46] Y. Yang, Y. Shi, M. Wan, W. H. Matthaeus, and S. Chen, Phys. Rev. E **93**, 061102(R) (2016).
[47] E. Camporeale, L. Sorriso-Valvo, F. Califano, and A. Retinò, Phys. Rev. Lett. **120**, 125101 (2018).
[48] S. S. Cerri and E. Camporeale, Phys. Plasmas **27**, 082102 (2020).
[49] N. T. Baker, A. Pothérat, L. Davoust, and F. Debray, Phys. Rev. Lett. **120**, 224502 (2018).
[50] C. G. Speziale, G. Erlebacher, T. Zang, M. Hussaini, and L. Sorriso-Valvo, Phys. Fluids **31**, 940 (1988).
[51] S. Zenitani, M. Hesse, A. Klimas, and M. Kuznetsova, Phys. Rev. Lett. **106**, 195003 (2011).
[52] Z. Xu, B. Qiao, H. X. Chang, W. P. Yao, S. Z. Wu, X. Q. Yan, C. T. Zhou, X. G. Wang, and X. T. He, Phys. Rev. E **93**, 033206 (2016).